

Overview of the MODIS Collection 6 Cloud Optical Property (MOD06) Retrieval Look-up Tables

version 1: June 28, 2017

GSFC Cloud Retrieval Product Team Points of Contact:
Nandana Amarasinghe, Steven Platnick, Kerry Meyer

1 Overview

The use of asymptotic theory for optically thick atmospheres in Collection 5 (C5) and earlier versions was replaced with a complete set of cloud reflectance and emissivity look-up tables (LUTs) containing a full range of cloud optical thickness (COT) and effective particle radius (CER) values. For optically thick atmospheres, the resulting reflectance computations are the same as those obtained from asymptotic theory, but this change simplifies the maintenance of the MOD06 code such that multiple paths (i.e., optically thin and optically thick atmospheres, followed by interpolation between them) are no longer required. In addition, more optically thin COTs values are included in the LUTs improving the quality of reflectances in that range. Further, the addition of ocean/water LUTs and separation of the cloud top bidirectional reflectance function (R) into single scattering (SS) and multiple scattering (MS) components is a significant difference between the C6 LUTs and those used in previous collections.

In order to minimize angular interpolation errors during the retrieval process, only the MS component to the cloud top bidirectional reflectance function is stored in the LUTs. During the retrieval process, the SS component is constructed dynamically (“on the fly”) from the phase function that is also stored in the LUT, and added to the MS component. The SS calculation uses the exact pixel-level angular information. The LUTs contain the MS component for six MODIS channels centered at 0.66, 0.87, 1.24, 1.63, 2.13, and 3.79 μm , as a function of COT, CER, cosines of the solar zenith (μ_0) and satellite viewing (μ) angles, and relative azimuth angle

Table 1. Range of Values of Look up table (LUT) parameters

Variable	# of grid points and Range
τ	34 (0, 159)
$r_e (\mu\text{m})$	18 [2,30] water phase 12 [5,60] ice phase
$\theta_0 (\text{deg})$	33 [0, 82)
$\theta (\text{deg})$	28 [0, 67)
$\Delta\phi (\text{deg})$	37 [0, 180]
$u(\text{ms}^{-1})$	3 {3,7,15}

between the sun and the satellite ($\Delta\phi$); separate LUTs are created for ocean/water surfaces with several wind speeds (u) and for land surfaces with a zero surface albedo. **Table 1** summarizes the number of grid points and the range of parameter values of the LUTs. Note that while the liquid and ice phase LUT CERs range from 2 to 30 μm and 5 to 90 μm , respectively, the allowable retrieval solution space for liquid and ice clouds are limited to 4 to 30 μm and 5 to 60 μm , respectively, for C6.

In addition, reflected flux, transmitted flux, and spherical albedo for the above six channels, as well as the IR channel centered at 11 μm , are also computed and included in the land LUT for use with a Lambertian surface whose albedo is included separately (Section 2.2). Ocean LUTs also contain effective surface and cloud emissivities for the channels centered at 3.7 and 11 μm ; for the land LUTs, these effective emissivities are calculated from the flux and spherical albedo data.

There are a total of 15 LUTs in HDF4 format. One LUT provides the phase function data needed for the single scattering calculation and other scattering properties for both phases. There are two LUTs for land retrievals (black albedo surface)—one for each phase—providing the MS reflectances and total reflectance standard derivations corresponding to the effective variance model uncertainty, as well as fluxes/albedos necessary for incorporating ancillary spectral surface albedos. There are 12 ocean LUTs—6 for each phase corresponding to 3 MS reflectance and flux/albedo/effective emissivity LUTs and 3 reflectance standard deviation LUTs representing the effective variance and wind direction error sources for the three wind speeds (3.0, 7.0, and 15.0 ms^{-1}).

2 Radiative Transfer Calculations

2.1 Phase Function Expansion with Legendre Polynomials

Forward radiative transfer calculations for the LUTs were performed with the discrete ordinates radiative transfer (DISORT) model developed by *Stamnes et al.* [1988, 2000], using 64 streams (NSTR=64) to characterize the upwelling and downwelling radiance (32 up and 32 down). To account for the wind speed/direction dependence of ocean surface bidirectional reflectance, we have incorporated into DISORT the Cox-Munk ocean bidirectional reflectance model implemented in libRadTran 1.4 [*Mayer and Kylling*, 2005]. Subsequently, we have conducted a thorough investigation of the accuracy and efficiency of DISORT (including the Cox-Munk ocean BRDF), and have modified its routines to achieve significant improvement in computational efficiency for simulations over ocean surfaces (see Appendix A).

For simulations over ocean surfaces, we assume an atmosphere-surface system consisting of three adjacent plane parallel homogeneous layers, and explicitly account for below-cloud Rayleigh scattering assuming a nominal profile of atmospheric pressure/altitude. The cloud is placed in the top layer, with a thickness of 1 km and a fixed altitude of 8 km above the surface for both liquid and ice phases. All below-cloud Rayleigh scattering, except for the contribution from the lowest atmospheric profile layer, are combined to form the second layer. The bottom

layer consists of the Rayleigh scattering contribution from the lowest atmospheric profile layer combined with a boundary-layer, coarse mode aerosol with an optical thickness of 0.1. The boundary layer aerosol radiative model (i.e., single scattering albedo, asymmetry parameter) is a coarse mode model used in the MOD04 Dark Target aerosol retrievals (see Table 2, aerosol mode 7, MOD04 ATBD [Levy *et al.*, 2009]); a Henyey-Greenstein model is assumed for the aerosol phase function. For simulations over land surfaces, the atmosphere-surface system consists of a single cloud layer overlying a black surface, i.e., zero surface albedo and no Rayleigh or aerosol layers. The land LUTs also contain fluxes and spherical albedos that allow for the incorporation of ancillary surface spectral albedo datasets (see Sect. 2.3). Note that above cloud atmospheric gaseous absorption is ignored in both the land and ocean LUT simulations, and is dynamically accounted for during the retrieval process using the retrieved cloud top pressure, ancillary atmospheric profiles, and a pre-computed two-way spectral transmittance

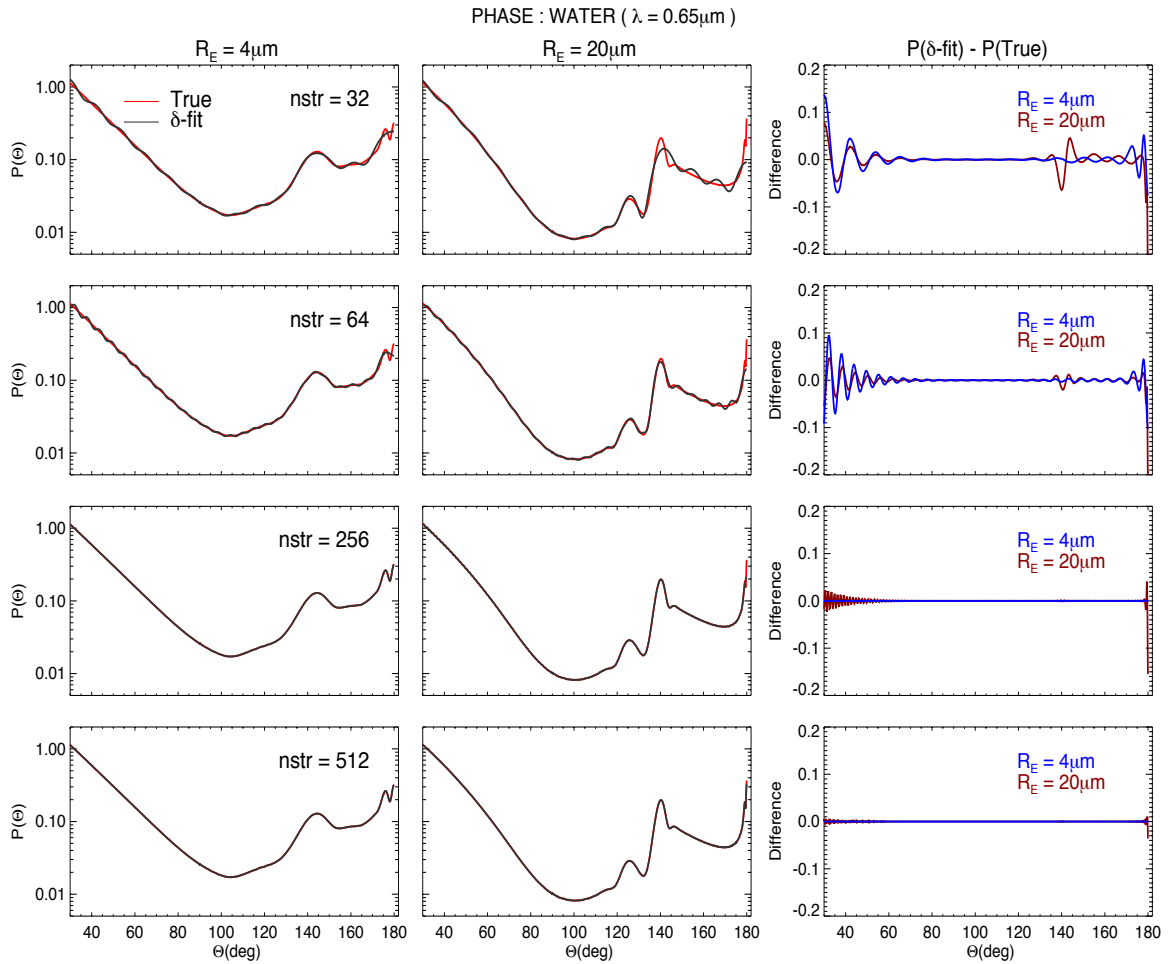


Figure 1. True phase function (red line), approximated phase function (black line), computed with 32, 64, 256, and 512 expansion coefficients and the difference (APPROXIMATED - TRUE, 3rd column) for MODIS band 1 ($0.66\mu\text{m}$) for liquid water clouds with $\text{CER}=4\mu\text{m}$ and $\text{CER}=20\mu\text{m}$

LUT; likewise, above cloud Rayleigh scattering at $0.66\ \mu\text{m}$ is dynamically accounted for on a pixel-level basis using the iterative approach of *Wang and King* [1997].

The single scattering properties of liquid water clouds are calculated from Mie theory, and are integrated over a Modified Gamma droplet size distribution,

$$n(r) = N_0 r^{(1-3v_e)/v_e} \exp\left(\frac{-r}{r_e v_e}\right) \quad (1)$$

assuming effective variance $v_e=0.10$. Complex refractive indices for liquid water are obtained from *Hale and Querry* [1973] for wavelengths in the range $0.25 \leq \lambda \leq 0.69\ \mu\text{m}$, *Palmer and Williams* [1974] for $0.69 < \lambda \leq 2.0\ \mu\text{m}$, and *Downing and Williams* [1975] for $\lambda > 2.0\ \mu\text{m}$. Single scattering properties of ice clouds are obtained from *Yang et al.* [2013] using the severely roughened aggregated column ice crystal habit, and are likewise integrated over a Modified Gamma size distribution (**Eq. 1**) with $v_e=0.10$. Computed single scattering properties (single scattering albedo, asymmetry parameter, extinction efficiency, phase function) for both ice and liquid water clouds are stored in the LUT. To approximate the forward peak of the liquid and ice

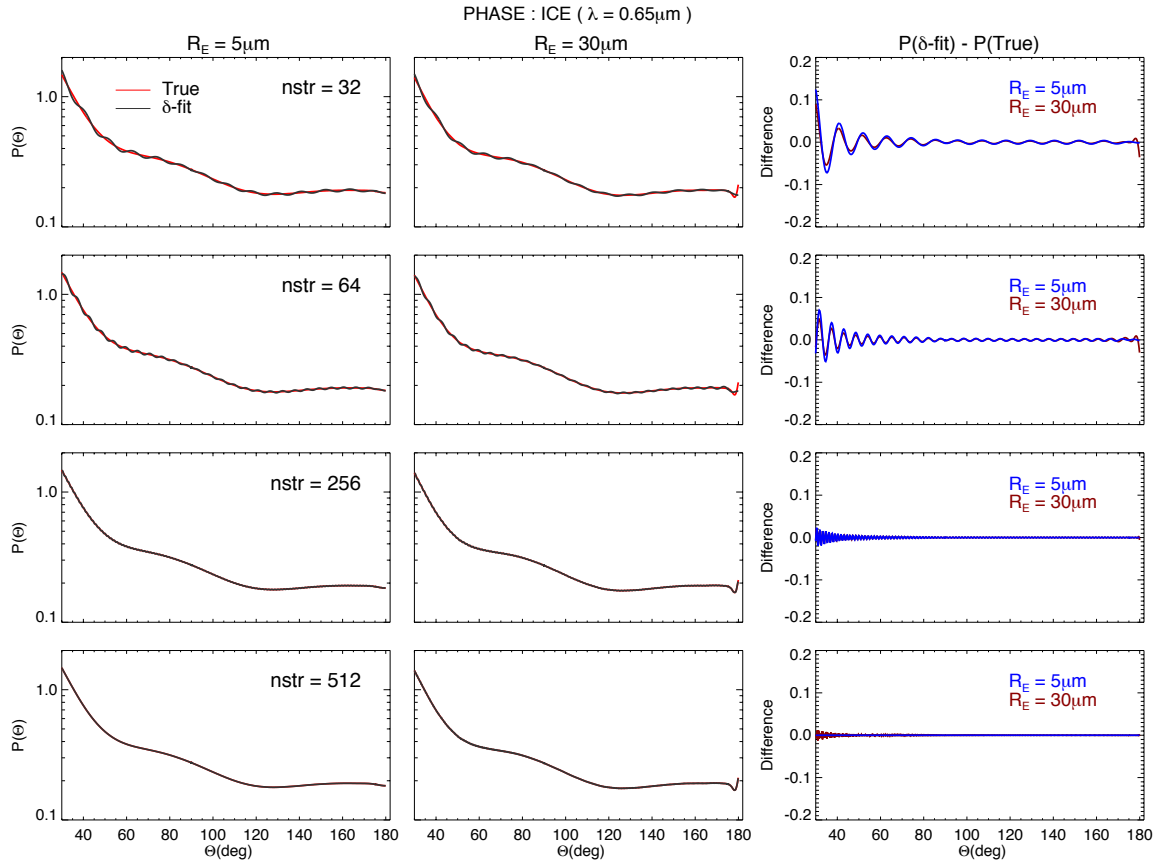


Figure 2. True phase function (red line), approximated phase function (black line), computed with 32, 64, 256, and 512 expansion coefficients and the difference (APPROXIMATED - TRUE, 3rd column) for MODIS band 1 ($0.66\ \mu\text{m}$) for ice clouds with $\text{CER}=5\ \mu\text{m}$ and $\text{CER} = 30\ \mu\text{m}$

phase functions for the radiative transfer calculations, the δ -fit method of *Hu et al.* [2000] is implemented to truncate the phase functions, which are then approximated by a 64-term Legendre polynomial expansion. **Figures 1 and 2** show the true phase function (red lines, left and middle columns) and approximated phase functions (black lines, left and middle columns) computed from 32-, 64-, 256-, and 512-term Legendre expansions (NSTR); also shown are the phase function differences (approximated–true) for liquid water clouds (Fig. 1) with CER=4 μm (blue lines, right column) and CER=20 μm (red lines, right column), and ice clouds (Fig. 2) with CER=5 μm and CER=30 μm . It is evident that increasing the number of expansion terms yields more accurate phase function approximation, though there continues to exist a significant difference between the true and approximated phase functions at back-scattering angles (glory region) for liquid water clouds, even with 512 expansion coefficients. This implies that if a high degree of accuracy is needed with regard to liquid water cloud total reflectance calculations at all angles from DISORT, one likely needs more than 512 phase function expansion terms, a computationally very intensive task that may not even be possible to achieve. However, as will be shown later by reflectance comparisons, removing the approximate single scattering component from DISORT total reflectance calculations that use a lower-order phase function expansion, and adding the exact single scattering back in using the true phase function, eases the need to resort to a higher number (≥ 512) of Legendre polynomial expansion coefficients.

Irrespective of the number of phase function expansion terms, the DISORT input parameters COT and single scattering albedo (ω_0) are adjusted with the phase function truncation factor f (i.e., the fraction of photons in the phase function forward peak due to diffraction), such that

$$\omega' = \frac{(1-f)\omega}{1-f\omega} \quad \tau' = (1-f\omega)\tau \quad (2)$$

where τ , denoting COT in some spectral channel λ_i , has been scaled to the MODIS 0.66 μm channel (λ_1) by

$$\tau_{\lambda_i} = \frac{Q_e(r_e, \lambda_i)}{Q_e(r_e, \lambda_1)} \tau_{\lambda_1} \quad (3)$$

2.2 Multiple Scattering (MS) Part of the Total Reflectance

The MS reflectance component is extracted from DISORT after the SS part, computed with approximated phase function PF , is subtracted from the total reflectance calculation following *Stamnes* [2000]. For a particular sun-satellite geometry, the SS component (R_{ss}) is calculated by interpolating the phase function, normalized to unity, in scattering angle space (Θ) and using the formula,

$$R_{SS}(\tau, r_e, \mu, \mu_0, \Delta\phi) = \frac{1}{4(\mu + \mu_0)} * \frac{\omega}{1-f\omega} * PF(\Theta, r_e) (1 - \exp[-\tau'(1/\mu + 1/\mu_0)]), \quad (4)$$

where r_e denotes CER. During the retrieval process the exact SS component is then added back dynamically to the interpolated MS component to obtain the total LUT reflectance.

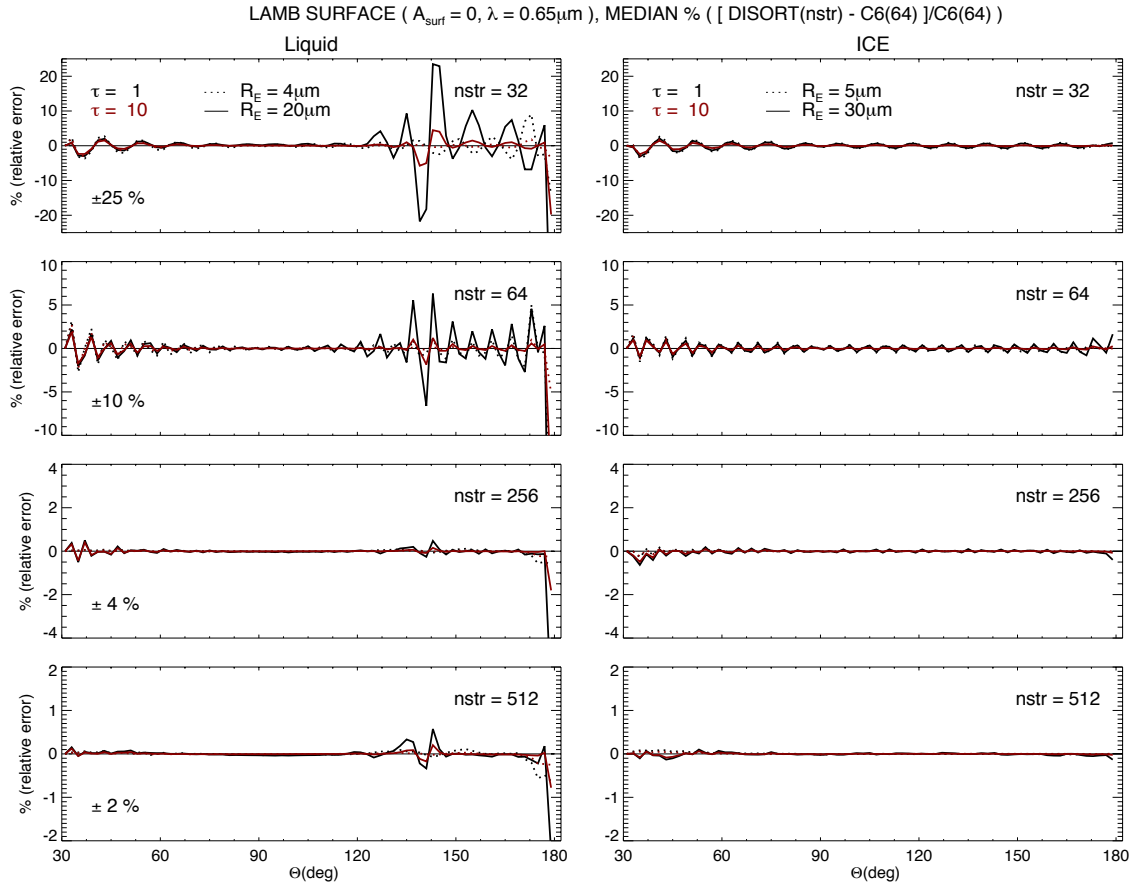


Figure 3. Median percent relative error between cloud-top reflectance computed from the C6 approach (MS(64)+SS) and that computed directly from DISORT with NSTR=32, 64, 256, and 512 for MODIS band 1 ($0.66\mu\text{m}$). Results are shown for liquid water clouds with CER= $4\mu\text{m}$ and $20\mu\text{m}$, and for ice clouds with CER= $5\mu\text{m}$ and $30\mu\text{m}$. Note that each row of plots have unequal y-axis limits.

Over land surfaces, a pixel-level Lambertian surface albedo is added to the LUT total cloud top reflectance R_0 following *King* [1987], such that

$$R_{A_g}(\tau, r_e, \mu, \mu_0, \Delta\phi) = R_0(\tau, r_e, \mu, \mu_0, \Delta\phi) + \frac{A_g t(\tau, r_e, \mu) \bar{r} t(\tau, r_e, \mu_0)}{1 - A_g \bar{r} t(\tau, r_e)}, \quad (5)$$

where t is the transmitted flux, \bar{r} is the spherical albedo, and A_g is the surface albedo. Over ocean/water surfaces, the MS reflectance component and effective cloud and surface emissivities are averaged over four vector wind directions (0° , 90° , 180° , 270°) to generate separate ocean LUTs for the three wind speeds (see Table 1).

For C6, we have chosen to use a 64-term Legendre expansion (NSTR=64) to approximate the phase function in the DISORT MS LUT computations. **Figure 3** shows the median of the percent relative difference between cloud-top reflectance computed from the C6 MS[64]+SS approach and total cloud-top reflectance computed directly using DISORT with NSTR=32, 64,

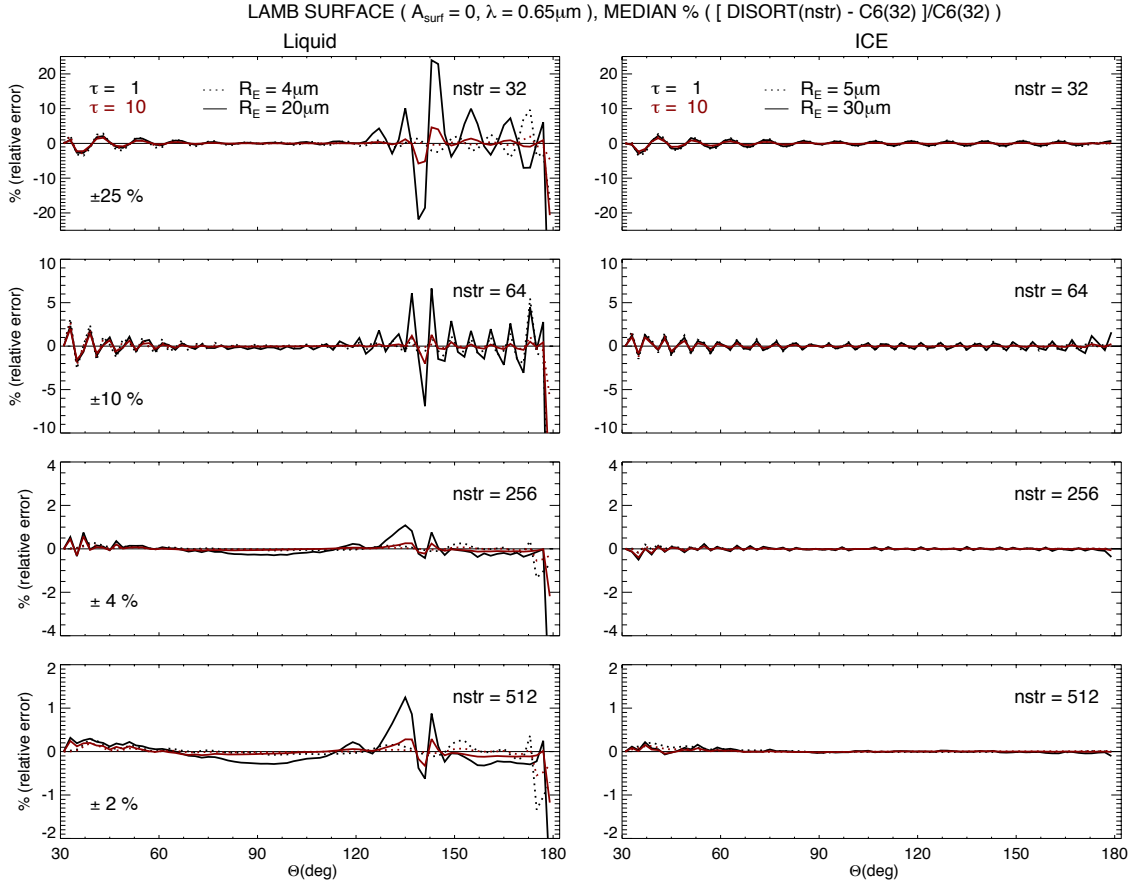


Figure 4. Same as Fig. 3, but MS reflectance is computed with NSTR=32, i.e., cloud-top reflectance from the C6 approach is $R = \text{MS}(32) + \text{SS}$

256 and 512. **Figure 4** is the same as Fig. 3, but the multiple scattering component is calculated with NSTR=32. Note that the reflectance differences seen here closely follow the PF differences seen in Figs. 1 and 3. It is evident that the cloud-top reflectance differences decrease as NSTR increases in the direct DISORT computations. Furthermore, assuming that the total reflectance computed directly from DISORT using NSTR=512 represents the true reflectance, the differences seen between it and the MS[64]+SS reflectance indicate that we can safely conclude that the C6 approach achieves a satisfactory level of accuracy (reflectance differences much less than 1% except at backscatter angles) while easing the burden of running DISORT with a large number of phase function expansion terms.

3 Discretization of LUT parameters and interpolation error

The SS component for a particular sun-satellite geometry is added dynamically to the interpolated MS component during the retrieval process. **Figure 5** illustrates the MS component and the total cloud top bidirectional reflectance (MS+SS) as a function of the cosine of the viewing zenith angle μ in the forward and backscattered directions for the $0.66\mu\text{m}$ channel

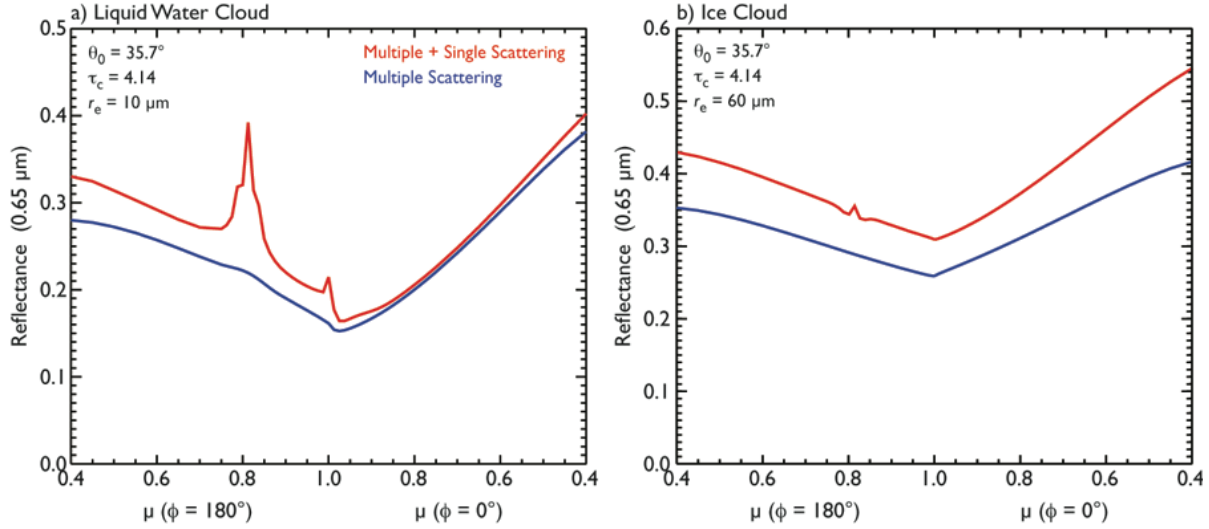


Figure 5. Total (red line) and MS (blue line) cloud-top reflectance for MODIS band 1 ($0.66\text{ }\mu\text{m}$) for (a) liquid water clouds with $\text{CER}=10\text{ }\mu\text{m}$, and (b) ice clouds (severely roughened aggregated columns) with $\text{CER}=60\text{ }\mu\text{m}$; all calculations assume $\text{COT}=4.14$ and $\mu_0=0.813$. The MS part of the reflectance is much smoother than the total reflectance that includes single plus multiple scattering. Note that the MS part of the reflectance function exhibits

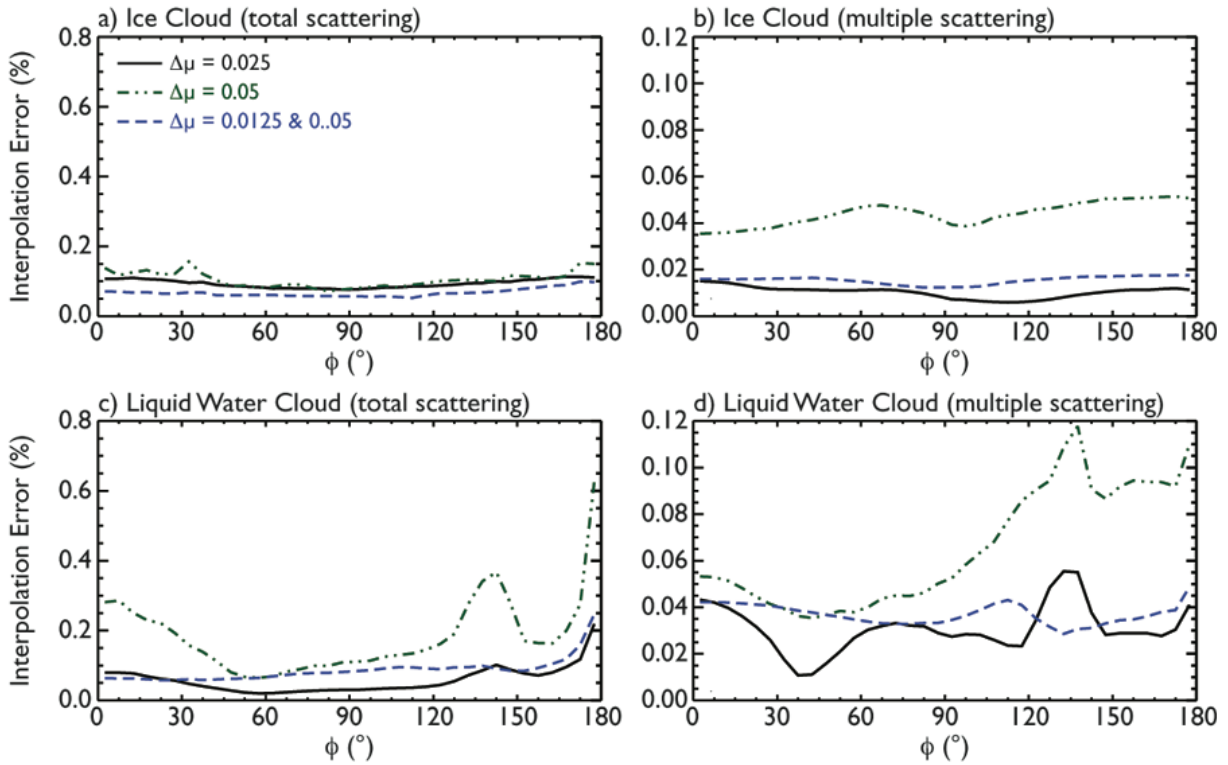


Figure 6. Median $0.66\text{ }\mu\text{m}$ LUT interpolation errors (averaged over all COT , CER , μ , and μ_0 entries) as a function of relative azimuth $\Delta\phi$ for three solar/view angle discretization schemes (see text). Shown are total reflectance (left column) and the MS component (right column) for ice clouds (severely roughened aggregated columns) with $\text{CER}=60\text{ }\mu\text{m}$ (top row) and liquid water clouds with $\text{CER}=10\text{ }\mu\text{m}$ (bottom row). Note the order of magnitude error reduction in the MS plots.

Table 2. Grid point values of the lookup table (LUT) parameters.

Quantity	# of points	Grid point values
COT	34	0.05, 0.10, 0.25, 0.5, 0.75, 1.0, 1.25, 1.5, 1.75, 2.0, 2.39, 2.87, 3.45, 4.14, 4.97, 6.0, 7.15, 8.58, 10.30, 12.36, 14.83, 17.80, 21.36, 25.63, 30.76, 36.91, 44.30, 53.16, 63.80, 76.56, 91.88, 110.26, 132.31, 158.78
CER (μm)	18 12	2, 4, 5, 6, 7, 8, 9, 10, 12, 14, 16, 18, 20, 22, 24, 26, 28, 30 (liquid water cloud) 5, 10, 15, 20, 25, 30, 35, 40, 45, 50, 55, 60 (ice cloud)
μ	28	0.40, 0.45, 0.50, 0.55, 0.60, 0.65, 0.70, 0.75, 0.7625, 0.7750, 0.7875, 0.8000, 0.8125, 0.8250, 0.8375, 0.8500, 0.8625, 0.8750, 0.8875, 0.900, 0.9125, 0.9250, 0.9375, 0.9500, 0.9625, 0.9750, 0.9875, 1.0
μ_0	33	0.15, 0.20, 0.25, 0.30, 0.35, 0.40, 0.45, 0.50, 0.55, 0.60, 0.65, 0.70, 0.75, 0.7625, 0.7750, 0.7875, 0.8000, 0.8125, 0.8250, 0.8375, 0.8500, 0.8625, 0.8750, 0.8875, 0.900, 0.9125, 0.9250, 0.9375, 0.9500, 0.9625, 0.9750, 0.9875, 1.0
$\Delta\phi$ ($^\circ$)	37	[0, 180] equally spaced with increments of 5°
u (ms^{-1})	3	3, 7, 15

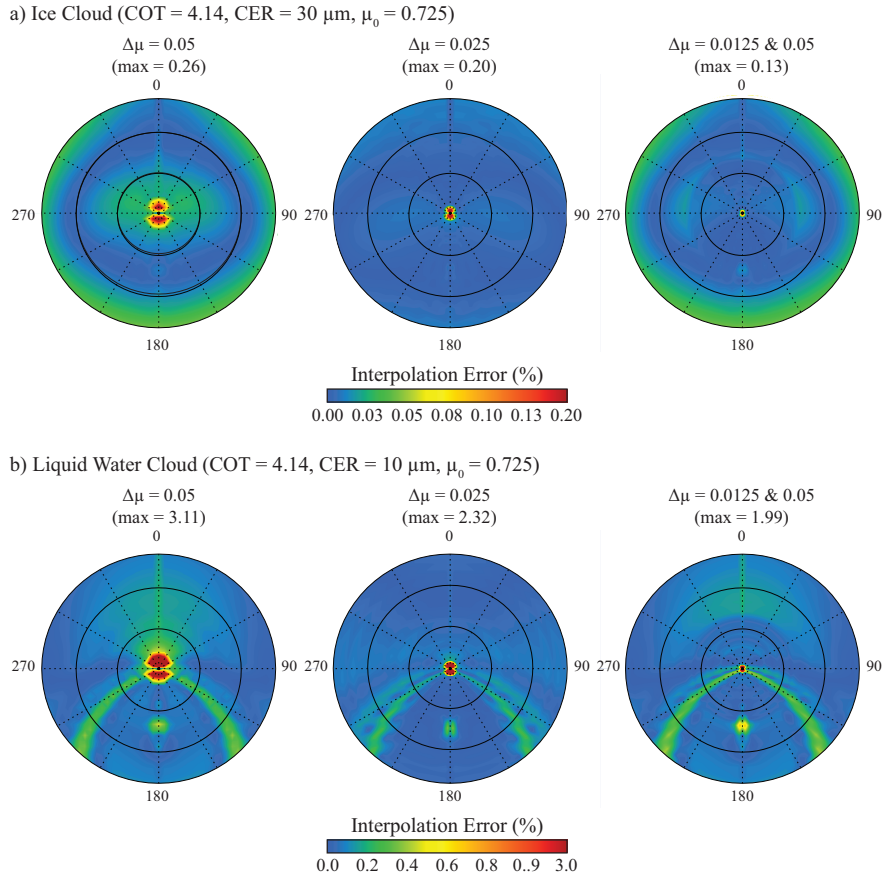


Figure 7. Maximum interpolation error for COT=4.14, $\theta_0=35^\circ$ for MS reflectances. The top row is for ice clouds with CER=30 μm (severely roughened aggregated columns), and the bottom row is for liquid water clouds with CER=10 μm . The hybrid discretization scheme (right column) has the least error near nadir.

(MODIS band 1). It is evident that the MS component (blue line) is a smoother function compared to the total reflectance (red line), implying that the SS component accounts for the angular structure of the total reflectance. Thus adding the exact SS component dynamically during the retrieval process acts to reduce LUT interpolation errors.

To further reduce interpolation errors, we conducted an exhaustive interpolation error analysis to determine the best discretization scheme for each dimension of the multi-dimensional LUTs. For COT, we followed the scheme suggested by *A. K. Heidinger* [2013, personal communication] in which COT values greater than 2 are discretized in equal intervals in log space. For solar and view angle space, multiple schemes were investigated. **Figure 6** shows the median interpolation error for full reflectance LUTs and MS reflectance LUTs with three different μ and μ_0 discretization schemes: (i) equally spaced with $\Delta\mu=0.025$, (ii) equally spaced with $\Delta\mu=0.05$, and (iii) a hybrid scheme with intervals of 0.0125 and 0.05 at larger and smaller μ , respectively (see **Table 2**). Comparing the interpolation error ranges (y-axes) associated with the total and MS reflectance LUTs, the interpolation error decreases by an order of magnitude when using the MS reflectance LUTs. Furthermore, the hybrid discretization scheme (broken blue lines in Fig. 6) produces the lowest maximum error for the MS LUTs, and also minimizes the interpolation error near $\mu=1.0$ as shown by the polar plots in **Figure 7**. As such, we implemented the hybrid discretization scheme for both solar and satellite zenith angles, while the relative azimuth angle is discretized in degree space. **Table 2** summarizes the grid points for COT, CER, μ , μ_0 and $\Delta\phi$ used in constructing the C6 LUTs.

4 Wind-speed Interpolated Ocean Bidirectional Reflectance Properties

4.1 Ocean Surface LUTs

LUTs for the reflection function of clouds overlying an ocean surface subject to non-isotropic reflection are now used. The ocean bidirectional reflectance model uses the wind speed and direction-dependent Cox-Munk wave-slope distribution [*Cox and Munk*, 1954]. Separate LUTs were calculated for three different wind speeds (3, 7, and 15 m s⁻¹), each one averaged over four vector wind directions (0, 90, 180, and 270° relative azimuth). Pigment concentration and salinity are set to 0.15 mg m⁻³ and 34 parts-per-thousand, respectively. A parameterization for white cap (foam) reflectance is taken from *Koepke* [1984]. Consequently, the LUTs now more accurately model the reflectance of optically thin clouds over the ocean that are sensitive to the non-isotropic sunglint distribution. In C5 and earlier collections, all reflectance of the underlying surface, both land and ocean, were modeled as Lambertian (isotropic), with a fixed ocean surface albedo $A_g=0.05$ that is characteristic of diffuse illumination. While the Lambertian ocean surface assumption is appropriate for sufficiently optically thick clouds, it is especially prone to errors for thin clouds near and away from sunglint. Our analysis shows that once COT becomes less than about 3, large differences are observed in cloud top reflectance between a Cox-Munk surface and a Lambertian surface with $A_g=0.05$. Consequently, the 10 m altitude

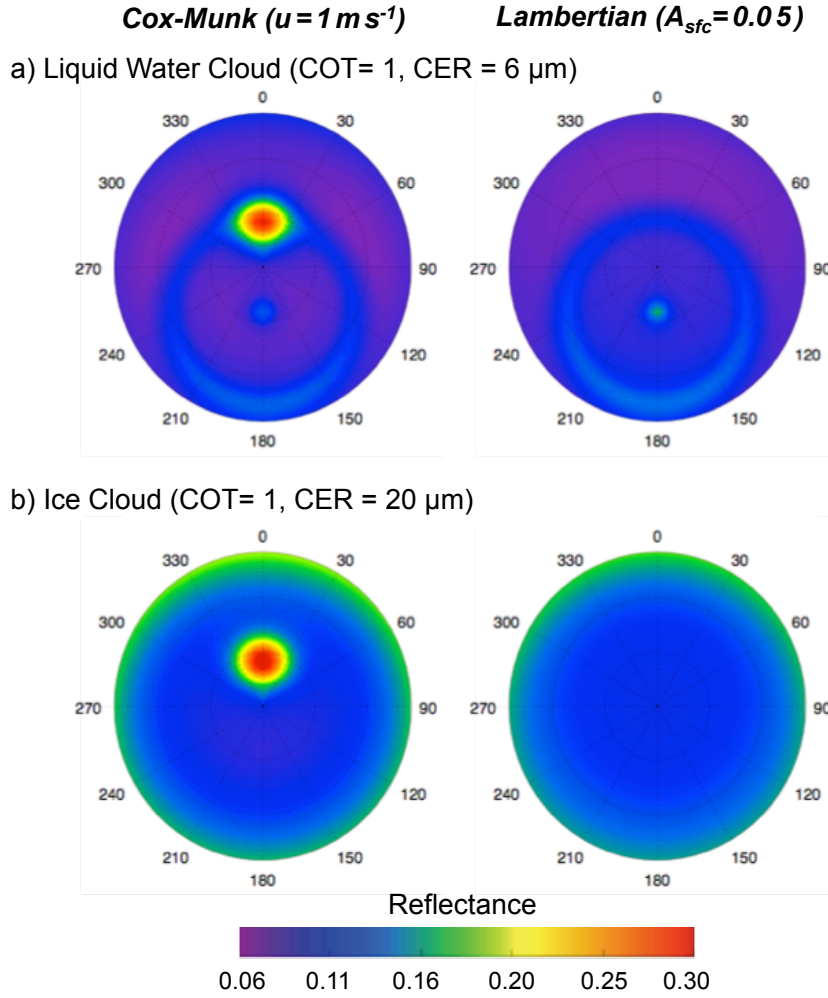


Figure 8. The angular cloud top distribution of reflectance in MODIS channel 1 ($0.66\mu\text{m}$) for COT=1 overlying the ocean surface for (a) liquid water clouds (CER=10 μm) and (b) C6 ice cloud model (CER=20 μm). The left-hand column applies to a Cox-Munk surface reflectance model with a wind speed of 1 m s^{-1} ; the right-hand column applies to a Lambertian surface reflectance model with a surface albedo of 0.05 (used in C5). The glory and rainbow scattering pattern for water clouds is evident.

wind speed over the ocean is now a required ancillary field and is obtained from the NCEP GDAS model.

Figure 8 shows calculations of the cloud-top bidirectional reflectance distribution function at $0.66\mu\text{m}$ (MODIS channel 1) for both (a) liquid water and (b) ice clouds overlying an ocean surface. The left-hand column applies to the Cox-Munk wave-slope distribution model and the right-hand column applies to a Lambertian ocean surface. The calculations are for a solar zenith angle $\theta_0 = 18.2^\circ$ and COT=1, with a wind speed of 1 m s^{-1} for the Cox-Munk model. With the Lambertian model, the cloud top reflectance is more isotropic, and generally brighter away from

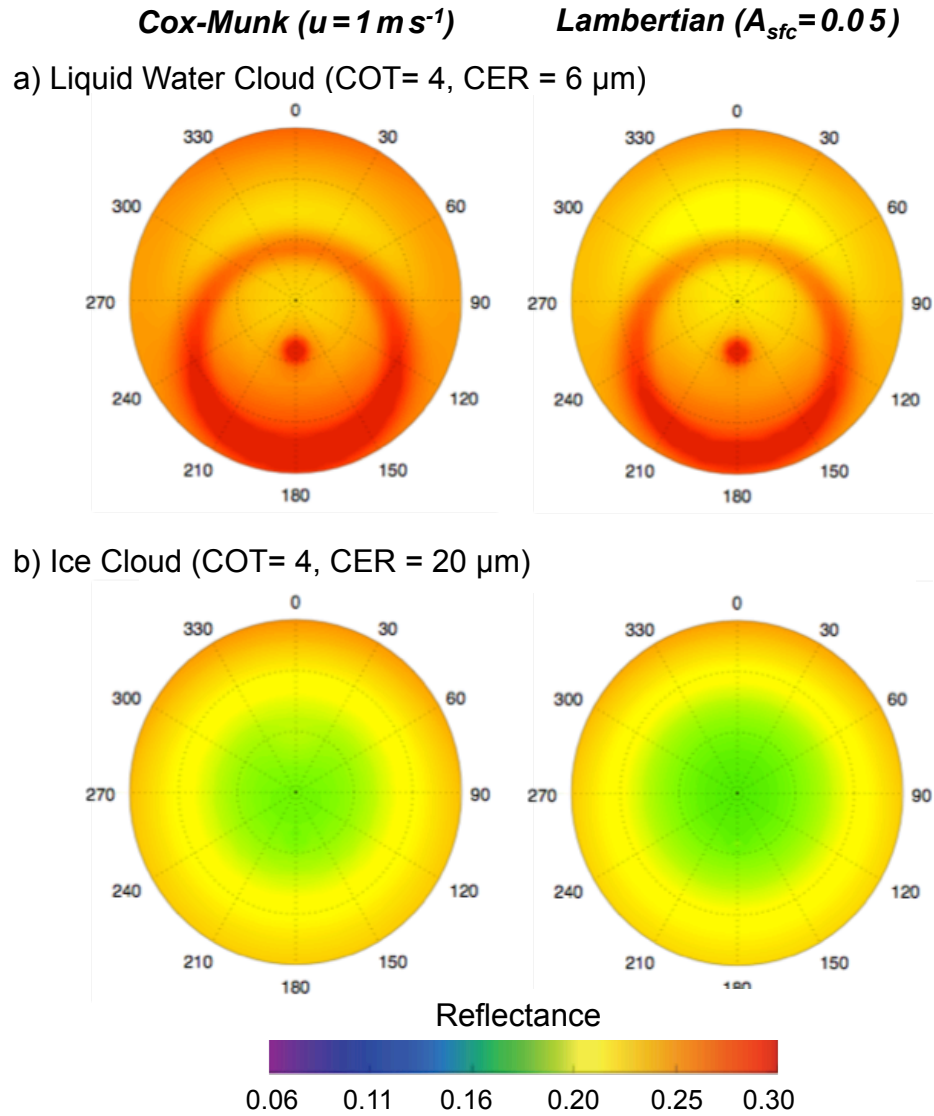


Figure 9. Same as Fig. 8 except COT=4.0.

sunglint, whereas for a more realistic Cox-Munk distribution the ocean reflectance is darker away from the sunglint angles. For optically thin clouds where sunglint and the ocean reflectance is more apparent, this modification to the surface scattering model leads to more accurate COT and CER retrievals, and generally fewer failed retrievals. **Figure 9** shows the same cloud-top reflectance distribution function but for COT=4. At this optical thickness, there is little distinction between the two surface models.

However, the accuracy of the Cox-Munk reflectance distribution for this application is not obvious given the practical need for ancillary ocean surface wind speed data (coarse resolution) over large geographic regions. An empirical evaluation of the model is shown in **Figure 10**. Here MODIS 0.87 μm clear sky reflectances are calculated for two MODIS Terra sunglint

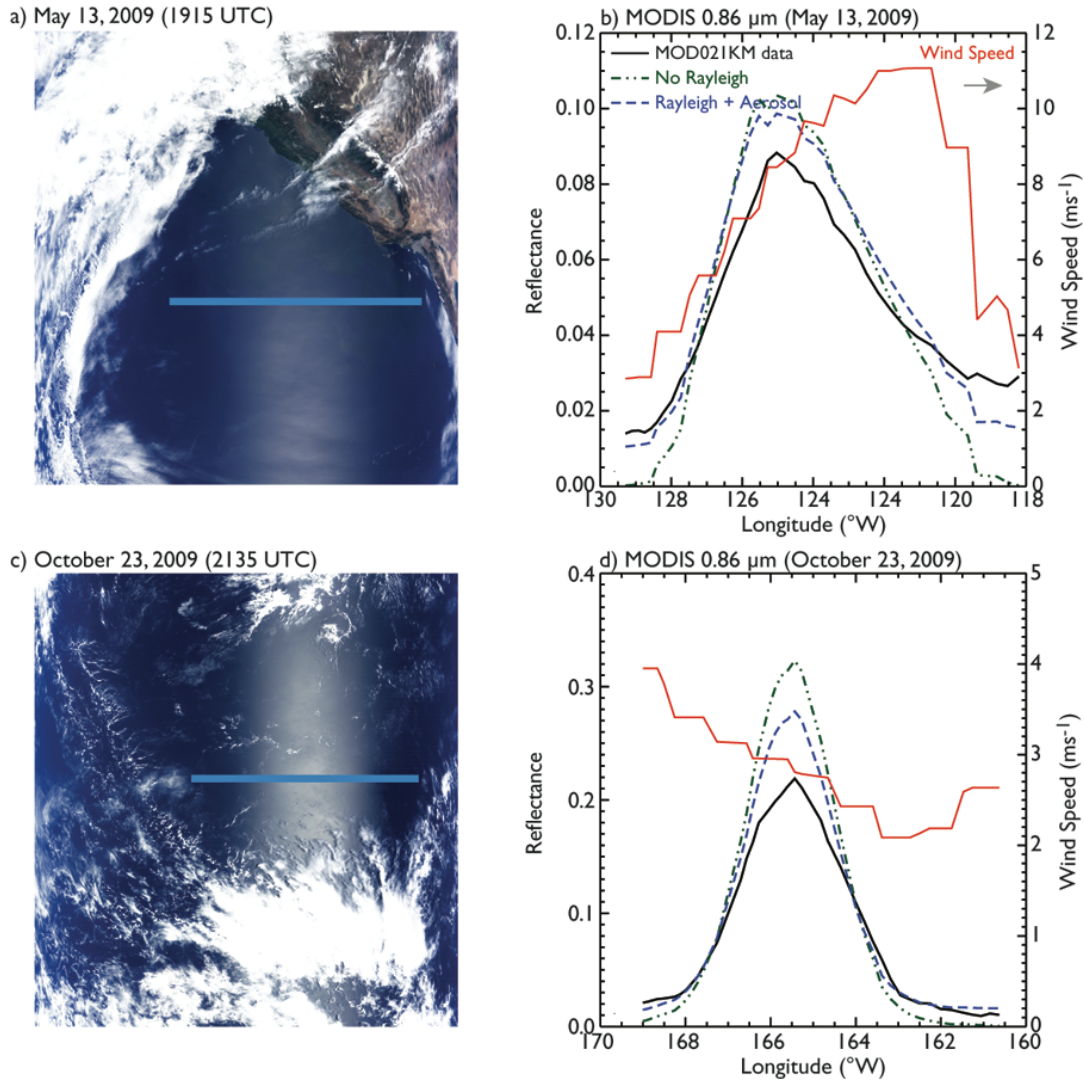


Figure 10. Cross section (blue rectangle) of the observed (solid black line) and calculated clear sky $0.87\mu\text{m}$ reflectances with the Cox-Munk surface bidirectional reflectance model for two MODIS Terra sunglint scenes. Ocean surface wind speeds are taken from NCEP GDAS reanalyses.

scenes. To understand the sensitivity to the clear sky atmospheric constituents, calculations are made with no Rayleigh scattering (green line) and Rayleigh scattering plus a coarse-mode sea-salt boundary layer aerosol model of optical thickness 0.1 (blue line). The average of five individual pixel scan lines (taken every 10th line) are used to compute the mean reflectance and angle information. Ocean surface wind speeds are temporally interpolated from the 1° NCEP GDAS 10m wind data for that day and location. The calculated reflectance compares well with the observations away from the glint, but there is a significant difference near the glint peak, especially for the October scene. Note that a default pristine aerosol optical depth (AOD) of 0.1 is used in calculating the ocean LUTs; it was found that the MOD04 AOD was nominally around 0.1 in the non-glint regions of these granules and therefore would not explain the differences. However, a reasonable match was obtained in both the glint peak and tail regions if the wind

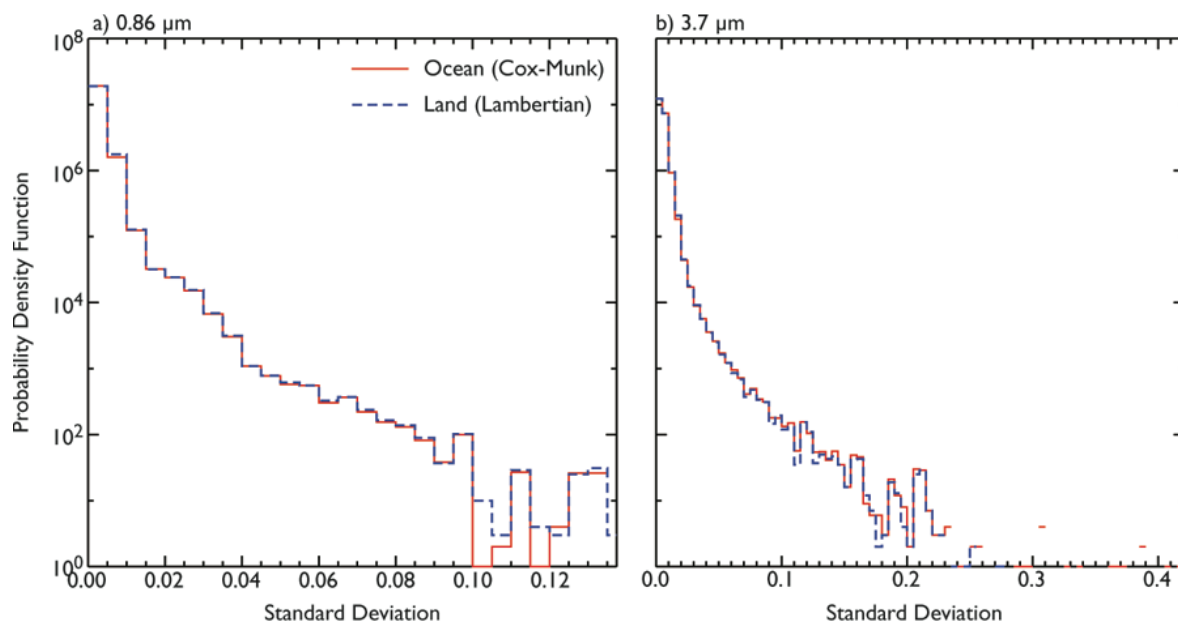


Figure 2.9-4. Histograms of standard deviation calculated for the ocean LUT with $u=3 \text{ ms}^{-1}$ (blue line) and from the land LUT (red line) for MODIS bands 2 and 20. No significant difference can be seen over about 3 orders of magnitude.

speed was increased by about 4 ms^{-1} and 1 ms^{-1} for the May and October granules, respectively (not plotted). This suggests caution in using thin cirrus and other small COT retrievals in sunglint, though surface sensitivity may be accounted for to some extent in the retrieval uncertainties that include a wind speed/direction error source. Regardless, using the Cox-Munk characterization of the ocean surface in C6 is a clear improvement over the previous 5% Lambertian reflector assumption.

4.2 Effective variance and wind direction uncertainties

To incorporate cloud radiative model errors in the retrieval uncertainty calculations, the total reflectances for clouds having particle size distributions with effective variances of 0.05 and 0.2 are also computed for both ice and liquid water. The effective variance error is then the standard deviation of the total reflectances corresponding to the three effective variances (including the default 0.1 value); these errors are included in the MS reflectance land LUTs. For ocean/water surfaces, the effective variance error is combined with a wind vector model uncertainty for each of the three LUT wind speeds, calculated as the standard deviation of the total reflectances corresponding to the 0° , 90° , 180° and 270° vector wind directions. The wind direction and effective variance errors are assumed to be independent, such that they are combined via a root-sum-square (RSS) calculation. **Figure 11** shows the histograms of the land (effective variance) and ocean (effective variance + wind direction) LUT model errors (i.e., reflectance standard deviations) for the MODIS 0.87 and $3.7 \mu\text{m}$ channels; note that the ocean errors are from the $u=3 \text{ ms}^{-1}$ LUT. Because there is no significant difference between the two histograms, to save computational time we decided to use the effective variance standard deviations from the land

LUTs for both land and ocean scenes instead of calculating the ocean standard deviations separately. Note that the net ocean LUT model uncertainty values are provided as separate LUTs due to file size constraints.

APPENDIX A. Changes made to the DISORT and the SURFAC routine with the Cox-Munk model from libRadTran 1.4

Modifications:

Accuracy

- NMUG (=50 in libRadTran 1.4), number of Gaussian quadrature points used in the integration to compute the Fourier coefficients of the surface bidirectional pattern, in SURFAC subroutine had to be increased to a larger value in order to avoid negative reflectances and oscillatory behavior. An example is given in the results section for NSTR=64 and $\mu = 0.1$. This fact has been noted in the SURFAC subroutine as “NSTR may be too small—to give an accurate approximation for the integration”. Presently, a user has to look inside the SURFAC subroutine to realize this fact and adjust NMUG accordingly.

Efficiency

- Used new Fortran 90 array operations to replace loop structures. May not make a difference if compiled with optimization (for Intel compiler used in testing).
- Cosines of the Fourier cosine series for each relative azimuth, $\cos(\text{MAZIM} * J)$, $\text{MAZIM} = 0, \text{NSTR}-1$, $J = 1, \text{NPHI}$, are calculated only once for a particular NSTR.
- Also, evaluating cosines, $\cos(\text{MAZIM} * \text{GMU}[K])$, $\text{MAZIM} = 0, \text{NSTR}-1$, $K = 1, \text{NMUG}$, with Gaussian quadrature points $\text{GMU}[K]$, inside the SURFAC routine is calculated only once and saved for later calls.
- SURFAC subroutine must be called for each azimuthal component (i.e. $\text{MAZIM} = 0, \text{NSTR}-1$). Inside the SURFAC subroutine, we identified the quantities that need to be calculated only during the first MAZIM loop (basically first call to DISORT) and saved those in an array for use in subsequent calls to DISORT. There are also unnecessary calls to BRDF routine inside SURFAC, during this first loop of $\text{MAZIM} = 0, \text{NSTR}-1$. Certain quantities need to be calculated calling BRDF routine only for $\text{MAZIM} = 0$. One can save these quantities for $\text{MAZIM} = 0$ and use them later during calls of $\text{MAZIM} = 1$ to $\text{NSTR}-1$. As an example, the original and a modified version of the loop that makes the very first call to BRDF from SURFAC are given in the Appendix. To implement these modifications efficiently, the convergence criterion (i.e., $\text{KCONV} \geq 2$, just after DO loop 170 in DISORT) is not applied during the very first call to DISORT. Depending on

the number of Gaussian quadrature points needed (NMUG in SURFAC) for calculating Fourier coefficients of surface BRDF, a significant improvement of efficiency is seen by implementing above changes.

- For our application, we improved the efficiency of library calculations further by saving quantities that depend on the input solar angles inside SURFAC (for an example, to run DISORT for several optical thicknesses and particle radii for the same set of solar angles). Implementation of this requires keeping track of the convergence cut-off of MAZIM in the main routine (DISORT). Cut-off of MAZIM may not be the same for all the optical thicknesses and radii. Therefore, one needs to keep track of this situation, and do the calculations and update saved arrays with respect to θ_0 and MAZIM inside the SURFAC routine.
- Inside SURFAC, all the saved arrays except the one with $\cos(\text{MAZIM} * * \text{GMU}[K])$ must be recomputed if any of the input parameters to the BRDF routine is changed. An IF-THEN-ENDIF block inside SURFAC handles this situation. This block needs to be updated if a new BRDF with new parameters is inserted into SURFAC.

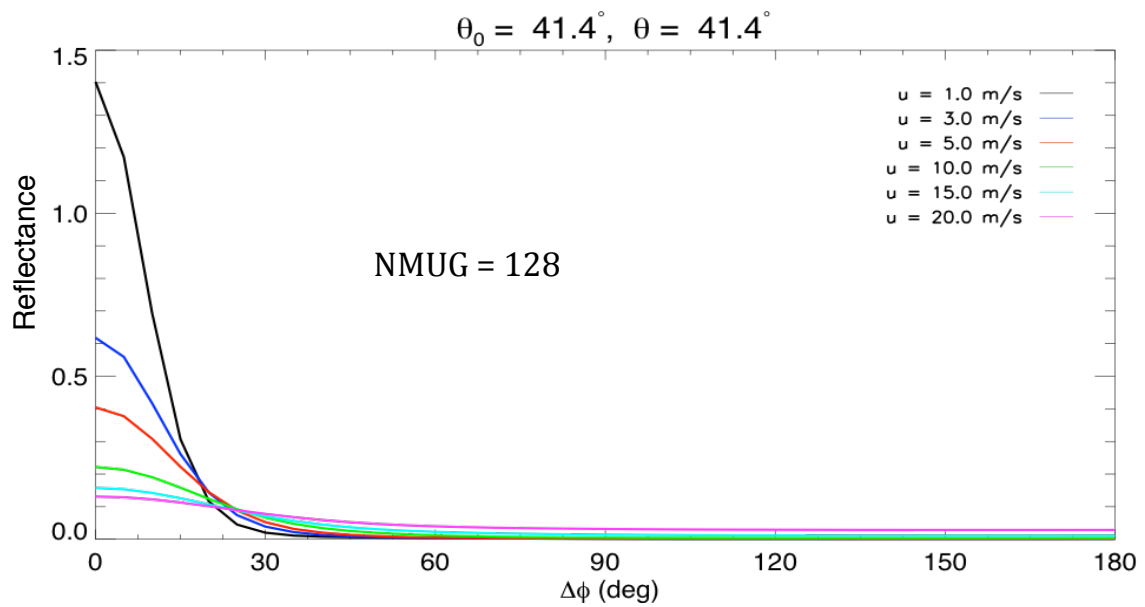
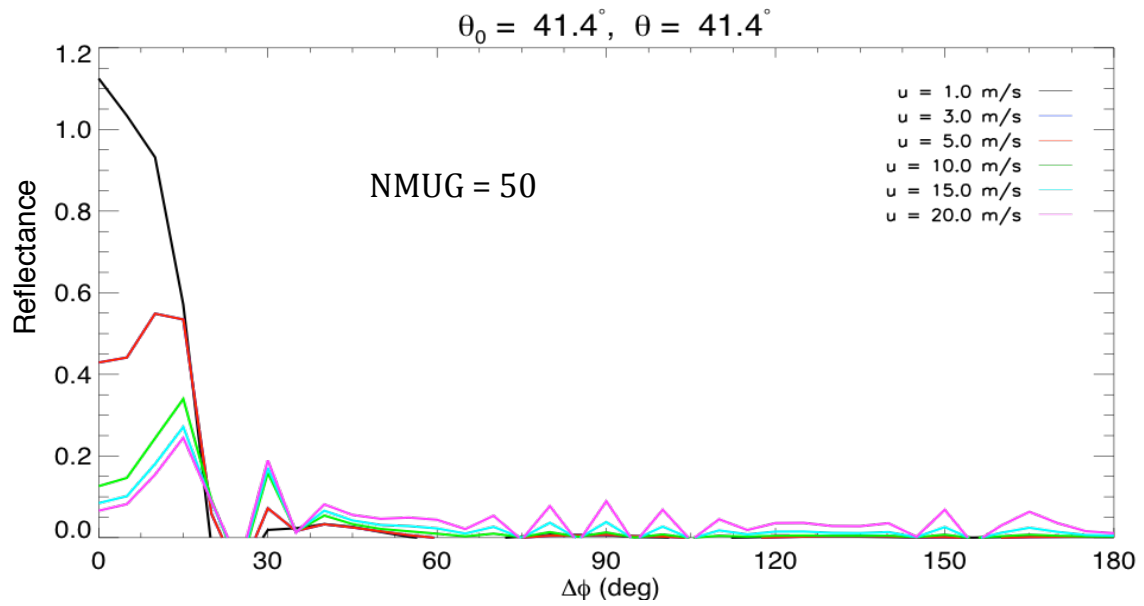
Results and Comparison:

Accuracy

- When NSTR = 64, following figures show the oscillatory behavior of reflectance with NMUG =50 and non oscillatory behavior with NMUG being increased to 128.

Efficiency

- Approximate CPU times (in seconds, single precision) for: (a) the rte solver in the original libRadTran 1.4, (b) libRadTran 1.4 with the above DISORT2 changes, (c) our stand-alone run of original DISORT2, and (d) our stand-alone run of DISORT2 with above changes. Calculations are for the solar angles given below with parameters $\lambda = 650 \text{ nm}$, $R_E = 6 \text{ m}$, $\tau = 2.0$, NSTR = 64, NMUG =128, wind speed = 3.0 m/s, 28 view angles, and 37 relative azimuth angles. These runs were done on a Mac with a single 2.66GHz Quad Core Intel Xeon processor and 8Gb of RAM. Since the number of terms required (cut-off in DISORT) in the Fourier sum decreases with decreasing solar zenith, CPU time also decreases.



Solar Zenith (Deg)	libRadTran 1.4 with DISORT2 RT Solver (Original) (Sec)	libRadTran 1.4 with Modified DISORT2 RT Solver (Sec)	DISORT2 RT Solver (Sec)	Modified DISORT2 RT Solver (Sec)
81.0	39.47	6.20	11.33	1.61
66.0	39.13	6.29	11.33	1.55

Solar Zenith (Deg)	libRadTran 1.4 with DISORT2 RT Solver (Original) (Sec)	libRadTran 1.4 with Modified DISORT2 RT Solver (Sec)	DISORT2 RT Solver (Sec)	Modified DISORT2 RT Solver (Sec)
36.0	27.21	4.90	11.33	1.55
9.0	10.63	3.55	11.32	1.55
0.0	2.90	2.92	1.08	1.08

- MODIS LUTs: DISORT2 with the original SURFAC subroutine in a stand-alone driver program, in double precision, took approximately 40 days to create our LUT's (7 channels, 3 wind speeds, 34 , 18 R_E, 33 μ_0 , 28 μ , 37 Δ), where as with the above implementations this task could be completed within 2 days on a single 2.66GHz Quad Core Intel Xeon processor.

SURFAC routine in DISORT:

The original and a modified version of the inner loop that makes the very first call to BRDF function from SURFAC are given below. Since input parameters to BRDF function do not depend on MAZIM, it will be called only for MAZIM = 0 and the returned value from BRDF function is saved for subsequent values of MAZIM loop in DISORT. Also, by saving MAZIM dependent quantity (array BDR) during the first call to DISORT, unnecessary calls to BRDF function during subsequent calls to DISORT are eliminated.

Original loop

```

DO 70 IQ = 1, NN

    DO 50 JQ = 1, NN

        SUM = 0.0
        DO 40 K = 1, NMUG
            SUM = SUM + GWT (K) *
&                BDREF (WVNMLO, WVNMHI, CMU (IQ), CMU (JQ),
&                PI*GMU (K)) * COS (MAZIM*PI*GMU ( K ) )
40        CONTINUE

        BDR (IQ, JQ) = 0.5 * (2. - DELM0) * SUM

```

50 CONTINUE

.
.
.

70 CONTINUE

Modified loop

DO 70 IQ = 1, NN

IF(firstCycle)THEN

!Calculations done for all MAZIM's. First call to DISORT

DO 50 JQ = 1, NN

RSUM = 0.0

IF (MAZIM == 0 .AND. MAZIMPREV == 9999) THEN

! Need to calculate only for MAZIM = 0, and redo for any

! Change in input parameters to BDREF

DO 40 K = 1, NMUG

& BDREFS3 (IQ, JQ, K)=BDREF_GC (WVNMLO, WVNMHI,
CMU (IQ), CMU (JQ), PI*GMU (K))

BDREFS3 (IQ, JQ, K)= BDREFS3 (IQ, JQ, K) * GWT (K)

& RSUM = RSUM + BDREFS3 (IQ, JQ, K) *
40 cosMazimGMUSaved(MAZIM,K)

CONTINUE

ELSE

& RSUM = SUM (BDREFS3 (IQ, JQ, 1:NMUG) *
cosMazimGMUSaved(MAZIM,1:NMUG))

ENDIF

BDR (IQ, JQ) = 0.5 * (2. - DELM0) * RSUM

BDRSAVED (MAZIM, IQ, JQ) = BDR (IQ, JQ) !save it for later use

!does not depend on mu0

50 CONTINUE

ELSE !FirstCycle

!Assigned from saved array for subsequent calls to DISORT

BDR (IQ, 1:NN) = BDRSAVED (MAZIM, IQ, 1:NN)

ENDIF !End firstcycle

References

- Baum, B. A., P. Yang, A. J. Heymsfield, S. Platnick, M. D. King, Y. X. Hu, and S. T. Bedka, 2005: Bulk scattering properties for the remote sensing of ice clouds. 2: Narrowband models. *J. Appl. Meteor.*, **44**, 1896-1911.
- Cox, C., and W. Munk, 1954: The measurements of the roughness of the sea surface from photographs of the sun's glitter. *J. Opt. Soc. Amer.*, **44**, 838-850.
- Downing, H. D., and D. Williams, 1975: Optical-constants of water in the infrared. *J. Geophys. Res.*, **80**, 1656-1661.
- Hale, G. M., and M. R. Querry, 1973: Optical constants of water in the 200-nm to 200- μ m wavelength region. *Appl. Opt.*, **12**, 555-563.
- Hu, Y. X., B. Wielicki, B. Lin, G. Gibson, S. C. Tsay, K. Stamnes, and T. Wong, 2000: Delta-Fit: A fast and accurate treatment of particle scattering phase functions with weighted singular-value decomposition least-squares fitting. *J. Quant. Spectrosc. Radiat. Trans.*, **65**, 681-690.
- Koepke, P., 1984: Effective reflectance of oceanic whitecaps," *Appl. Opt.*, **23**, 1816-1824.
- King, M. D., 1987: Determination of the scaled optical thickness of clouds from reflected solar radiation measurements. *J. Atmos. Sci.*, **44**, 1734-1751.
- King, M. D., S. C. Tsay, S. E. Platnick, M. Wang and K. N. Liou, 1997: *Cloud Retrieval: Algorithms for MODIS: Optical Thickness, Effective Particle Radius, and Thermodynamic Phase*. Algorithm Theoretical Basis Document ATBD-MOD-05, 79 pp., modis-atmos.gsfc.nasa.gov/reference_atbd.html.
- Koepke, P., 1984: Effective reflectance of oceanic whitecaps. *Appl. Opt.*, **23**, 1816-1824.
- Levy, R. C., L. A. Remer, D. Tanré, S. Mattoo, and Y. J. Kaufman, 2009: *Algorithm for remote sensing of tropospheric aerosol over dark targets from MODIS: Collections 005 and 051*, Algorithm Theoretical Basis Document ATBD-MOD-04, 96 pp., modis-atmos.gsfc.nasa.gov/reference_atbd.html.

atmos.gsfc.nasa.gov/reference_atbd.html.

- Mayer, B., and A. Kylling, 2005: Technical note: The libRadtran software package for radiative transfer calculations - description and examples of use. *Atmos. Chem. Phys.*, **5**, 1855-1877.
- Palmer, K. F., and D. Williams, 1974: Optical properties of water in the near infrared. *J. Opt. Soc. Amer.*, **64**, 1107-1110.
- Stamnes, K., S. C. Tsay, W. Wiscombe, and K. Jayaweera, 1988: A numerically stable algorithm for discrete-ordinate-method radiative transfer in multiple scattering and emitting layered media. *Appl. Opt.*, **27**, 2502-2509.
- Stamnes, K., S. C. Tsay, W. Wiscombe, and I. Laszlo, 2000: DISORT, a General-Purpose Fortran Program for Discrete-Ordinate-Method Radiative Transfer in Scattering and Emitting Layered Media : Documentation of Methodology.
- Yang, P., L. Bi, B. A. Baum, K. N. Liou, G. W. Kattawar, M. I. Mishchenko, and B. Cole, 2013: Spectrally consistent scattering, absorption, and polarization properties of atmospheric ice crystals at wavelengths from 0.2 to 100 μm . *J. Atmos. Sci.*, **70**, 330–347.
- Wang, M., and M. D. King, 1997, Correction of Rayleigh scattering effects in cloud optical thickness retrievals, *J. Geophys. Res.*, **102**, 25915-25926.